14

Cherenkov ring imaging

14.1 Introduction

Charged particles traversing a medium with a velocity exceeding the velocity of light in the material emit a coherent front of electromagnetic radiation, an effect discovered in the thirties by Pavel Cherenkov, Nobel laureate in physics 1958. Detection of the photons emitted by the Cherenkov effect provides information on the particle's velocity; combined with an independent measurement of total energy or magnetic deflection, it helps in identifying the mass of the particle. Although the emission occurs over the whole spectrum, photons can only be detected within the wavelength interval for which the medium is transparent.

The effect is widely exploited in particle physics for particle identification in specific ranges of mass and velocity, deploying a succession of radiators with different index of refraction; using photomultipliers as photon detectors, threshold Cherenkov counters have a limited angular acceptance, and are used mainly for particle tagging of un-separated high energy beams.

Above the threshold, the angle of emission of photons depends on the particle velocity. In early devices exploiting the measurement of the emission angle, named differential Cherenkov counters, optical means restrict the detection of photons with ring-shaped diaphragms, and are therefore sensitive in a well-defined range of velocity; more sophisticated methods for detecting and localizing individual photons over a wider angular range have been attempted, using various systems of image intensifiers, but are limited in use due to their high cost and narrow angular coverage. For a review of classic Cherenkov counter techniques see Benot *et al.* (1972); Litt and Meunier (1973); and Gilmore (1980).

The development in the early 1970s of large-area position-sensitive detectors opened up new possibilities. Filled with a photosensitive vapour and operated at high gains, MWPCs could be used to detect and localize single photons in the ultra-violet (UV) domain, as proposed in the late seventies by the seminal work of

https://doi.org/10.1017/9781009291200.016 Published online by Cambridge University Press

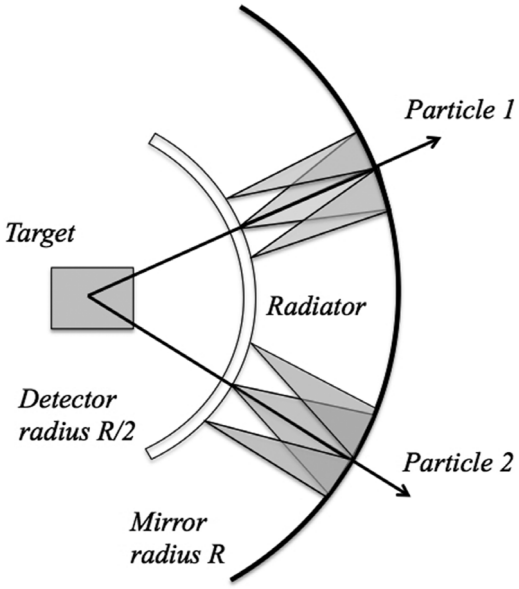

Figure 14.1 Schematics of a ring imaging Cherenkov detector (Seguinot and Ypsilantis 1977. By kind permission of Elsevier.

Jacques Séguinot and Thomas Ypsilantis (Seguinot and Ypsilantis, 1977). The cone of photons emitted in a radiator by charged particles above the Cherenkov threshold can be reflected in a ring pattern on a detector in the focal plane of a spherical mirror, Figure 14.1, or detected directly with the so-called proximity focussing geometry (Figure 14.2). In both cases, a measurement of the ring radius provides information on the particle's velocity; more dispersive, proximity focusing requires the use of thin liquid or solid radiators with large values of the refractive index. The two methods are often combined within the same detector with different radiators, to extend the velocity range of identification, Figure 14.3.

To be exploited, the method requires finding a gas with a photo-ionization threshold lower than the transparency cut-off of the windows separating detector and radiator. In the original proposal, the choice was the use of lithium fluoride windows, expensive and easily damaged by exposure to moisture, with acetone or benzene as additives to the gas. Further work by the same authors identified triethyl amine (TEA), with a photo-ionization threshold around 7.6 eV, as a more convenient choice (Séguinot *et al.*, 1980). Combined with easily available and stable calcium fluoride windows, it permits one to attain quantum efficiency close to 50% at the peak of the window transparency region.

The discovery of a compound, TMAE, with even lower photo-ionization threshold (~5 eV) (Anderson, 1980) and the later development of solid caesium

https://doi.org/10.1017/9781009291200.016 Published online by Cambridge University Press

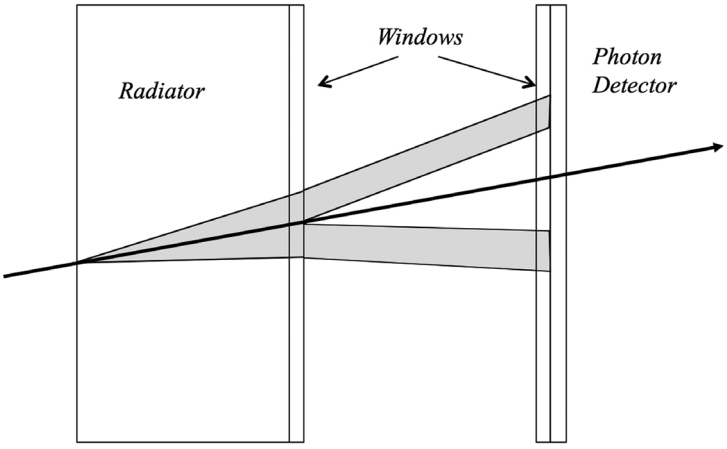

Figure 14.2 Proximity focusing RICH.

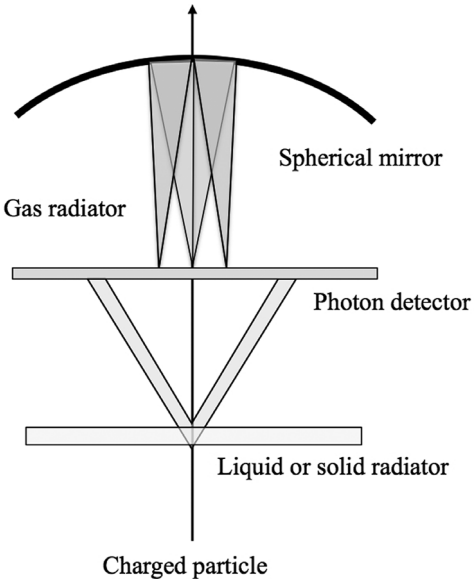

Figure 14.3 Combined gas ring imager and proximity focusing on a single photon detector.

iodide photocathodes that allowed one to use fused silica windows, easily available in large sizes, permitted the conception and construction of the large ring imaging Cherenkov counters (RICH)[1] particle identification systems that are described in the next sections.

[1] Also named CRID (Cherenkov ring imaging detectors)

https://doi.org/10.1017/9781009291200.016 Published online by Cambridge University Press

Table 14.1 *Radiators: transparency cut-off energy* E_{TC}*, index of refraction* n *or* (n − *1), Cherenkov threshold velocity* γ_T*, maximum emission angle* θ_M *and photons per cm of radiator at saturation* N_{PH} *detected with a figure of merit* $N_0 = 80\ cm^{-1}$.

Gases (NTP)	E_{TC} (eV)	$(n\text{-}1)10^6$ (at 7eV)	γ_T	θ_M (°)	N_{PH} /cm
He		33	123	0.48	0.005
Ne		67.3	86	0.66	0.01
Ar	16	300	41	1.4	0.05
CH_4	8.6	510	31	1.83	0.08
CF_4	12.5	488	32	1.80	0.08
C_2F_6		793	25	2.28	0.13
i-C_4H_{10}	8.3	1500	18		0.24
Liquids (NTP)		***n* (at 6.5 eV)**			
C_5F_{12}	7.5	1.262	1.638	37.6	30
C_6F_{14}	8.3	1.278	1.606	38.5	31
Solids		***n* (5.5 eV)**			
LiF	11.6	1.42	1.41	45.2	43
MgF_2	10.8	1.41	1.41	44.8	40
CaF_2	10	1.47	1.36	47.1	43
Fused silica	7.5	1.52	1.33	48.8	45

Table 14.2 *Photo-ionization threshold energy* E_T*, peak quantum efficiency of photosensitive compounds QE and vapour pressure* P *at NTP (QE values depend on sources).*

	E_T (eV)	Peak QE (%)	*P* (NTP) (Torr)
Acetone	9.65	31	251
TEA $(C_2H_5)_3N$	7.5	33–42	73.2
TMAE $C_2[(CH_3)_2N]_4$	5.3	29–40	0.50
Caesium iodide CsI	5.9	20–35	$<10^{-5}$

Values of quantum efficiency of vapours and transparency of gases and window materials are covered in detail in Chapter 3. Compiled from different sources, Table 14.1 and Table 14.2 summarize some useful parameters for widely used components in the realization of RICH counters (Gray, 1963; Ekelöf, 1984; Nappi and Seguinot, 2005). It should be noted that often values differ depending on sources, measurement conditions and the presence of trace pollutants. Several works describe the purification systems and methods of use of the fluorocarbon fluids used as radiators (Albrecht *et al.*, 2003; Wiedner *et al.*, 2008; Ullaland, 2005; Hallewell, 2011).

By inspection of the tables, one can see that using TEA as photoionising vapour ($E_T = 7.5$ eV), the choice of radiators is restricted to gases and

https://doi.org/10.1017/9781009291200.016 Published online by Cambridge University Press

fluoride crystals; with TMAE or solid CsI the range extends to fluorinated liquids, covering a wider region of refractivity and therefore of threshold velocity.

14.2 Recalls of Cherenkov ring imaging theory

Only some basic expressions are given here; detailed discussions of the theory and practice of the ring imaging technology can be found in many reviews (Ypsilantis, 1981; Arnold *et al.*, 1992; Seguinot and Ypsilantis, 1994; Ypsilantis and Seguinot, 1994; Nappi and Seguinot, 2005; Dalla Torre, 2011).

A charged particle traversing an optical medium with refractive index n emits a Cherenkov radiation when its relativistic velocity β exceeds a threshold value $\beta_T = 1/n$. The angle of emission θ relative to the particle direction is:

$$\cos\theta = 1/n\beta, \tag{14.1}$$

reaching a maximum value for $\beta \to 1$:

$$\theta_{\mathrm{MAX}} = \cos^{-1}\frac{1}{n}. \tag{14.2}$$

Computed from expression (14.1), Figure 14.4 shows the dependence of the Cherenkov angle on the particle velocity and several values of refractive index; large values of n result in low thresholds and large emission angles, and conversely for small values.

The number of photons emitted in the energy interval ΔE is given by the Frank–Tamm expression:

$$\frac{\Delta N}{\Delta E} = \left(\frac{\alpha}{\hbar c}\right) Z^2 L \sin^2\theta = \left(\frac{\alpha}{\hbar c}\right) Z^2 L \left[1 - \left(1 - \frac{n}{\beta}\right)^2\right], \tag{14.3}$$

where α is the fine structure constant, $\hbar$ Plank's reduced constant and Z and L the particle's charge and path length in the radiator.

Over the narrow wavelength interval between the window's transparency cut-off and the detector's photo-ionization threshold, for which n can be considered constant, integration of expression (14.3) gives a simple expression for the number of detected photons:

$$N = N_0 Z^2 L \sin^2\theta, \tag{14.4}$$

where the figure of merit N_0, characteristic of each detector, depends on the detector efficiency ε_{D}, the reflectivity of the mirror ε_{R}, and the optical transmission ε_{T}, all functions of the photon energy; it can be computed by integration over the

https://doi.org/10.1017/9781009291200.016 Published online by Cambridge University Press

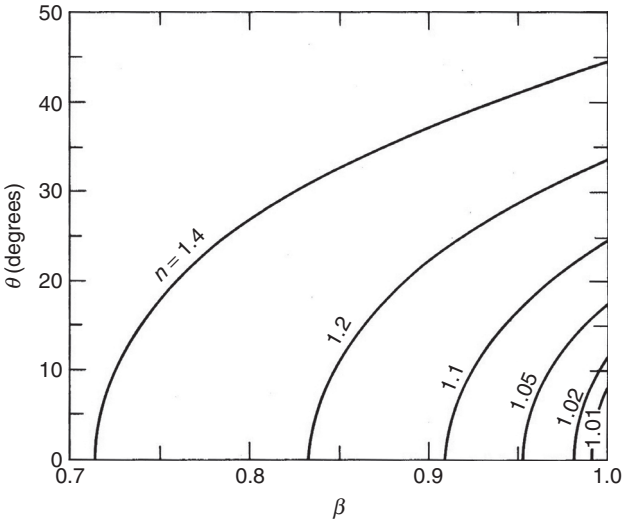

Figure 14.4 Cherenkov emission angle as a function of velocity for several values of the medium's index of refraction.

spectral sensitivity range, between the photo-ionization threshold and the window transparency cut-off:

$$N_0 = \frac{1}{137\hbar c}\int_{E_1}^{E_2} \varepsilon_D(E)\varepsilon_R(E)\varepsilon_T(E)\mathrm{d}E. \tag{14.5}$$

Typical values of the parameter N_0 for RICH detectors are between 50 and 100 photons/cm.

For an ideal optical system such as the one shown in Figure 14.1, the relative velocity resolution for N detected photons is given by:

$$\frac{\Delta\gamma}{\gamma} = \frac{\gamma^2\beta^2 n}{\sqrt{N_0}L}\Delta\theta, \gamma = 1/\sqrt{(1-\beta^2)}, \quad \Delta\theta = \Delta\theta_1/\sqrt{N}, \tag{14.6}$$

where $\Delta\theta_1$ is the single photon angular error, that includes all dispersive effects: the photon and particle direction localization, geometrical and optical aberrations. At high photon energies, an unavoidable contribution is the chromatic aberration caused by the dependence of the index of refraction of the medium on the wavelength of the emitted photons. The wavelength dependence of the refractive index in argon is given in Figure 14.5 (Langhoff and Karplus, 1969); the refractive index of fluoride crystals, used as detector windows or solid radiators, is shown in Figure 14.6 (Gray, 1963; Roessler and Walker, 1967). Insets in the figures provide

https://doi.org/10.1017/9781009291200.016 Published online by Cambridge University Press

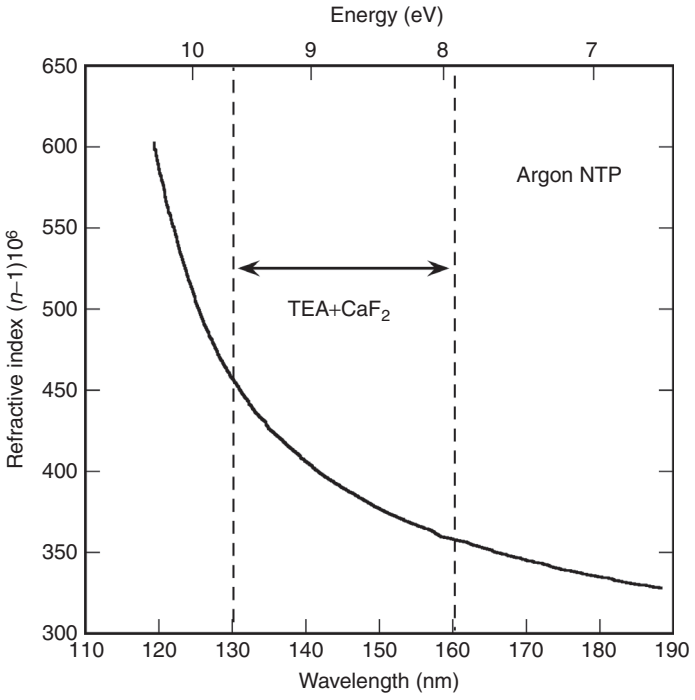

Figure 14.5: Wavelength dependence of the refractive index in argon. Data from Langhoff and Karplus (1969).

the approximate regions of sensitivity for a detector using TEA as photosensitive vapour and a calcium fluoride window, and respectively quartz windows and TMAE or CsI as photosensitive agents. A compilation of refractive index values as a function of wavelength for gases and liquids is given in Ullaland (2005); Figure 14.7 is an example of the dependence for several fluorocarbons used as radiators.

For optimal RICH detector performance, the various dispersive contributions should be minimized. Figure 14.8 is an example of computed dependence of the single photon angular resolution on three dispersive sources for a proximity focusing detector with a CsI photocathode, as a function of the Cherenkov angle and for two values of the particle incidence angle (Nappi and Seguinot, 2005).

The optimization depends on the detector geometry and operating parameters, and determines the particle identification power of the detector. Figure 14.9 gives a representative example of computed resolution of a TEA-operated RICH device with a 50 cm long, 10 atmosphere argon radiator and a 50 cm focal length mirror; the right scale gives the expected number of detected photons per ring (Charpak *et al.*, 1979a).

https://doi.org/10.1017/9781009291200.016 Published online by Cambridge University Press

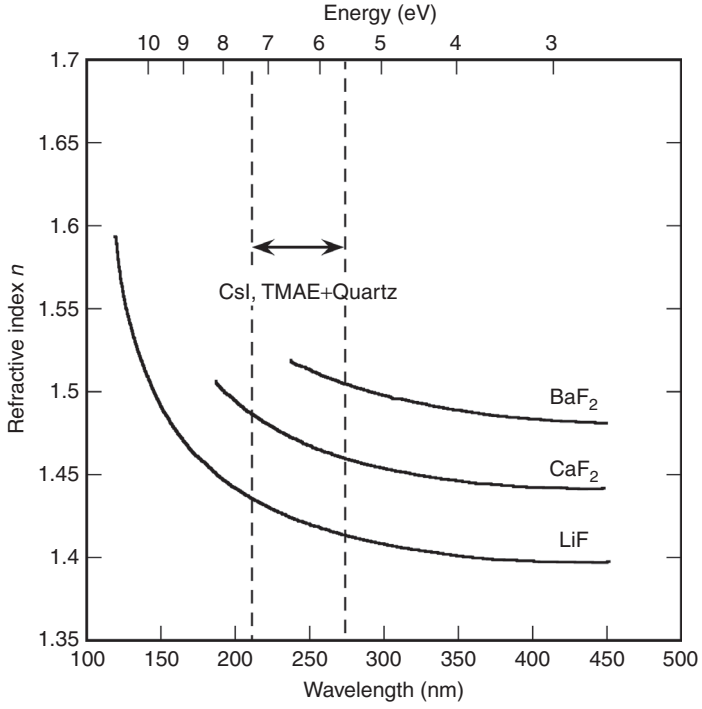

Figure 14.6 Wavelength dependence of the index of refraction of fluorides. Data from Gray (1963) and Roessler and Walker (1967).

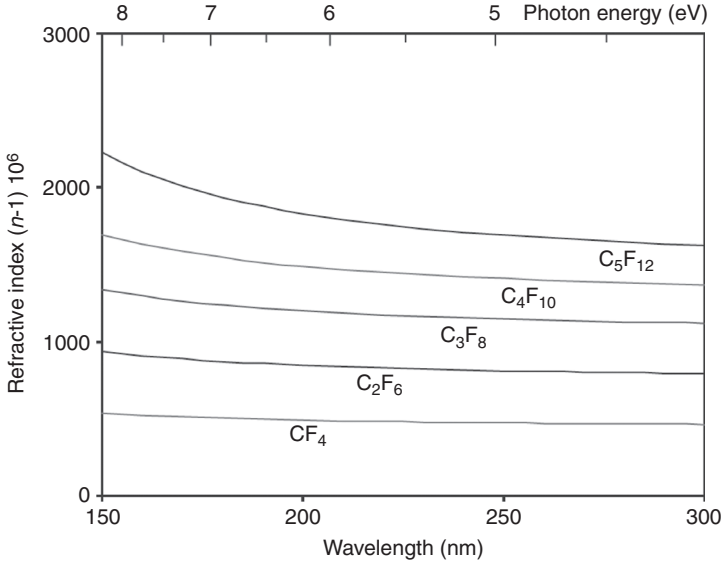

Figure 14.7 Index of refraction of *n*-perfluorocarbons as a function of wavelength (Ullaland, 2005). By kind permission of Elsevier.

https://doi.org/10.1017/9781009291200.016 Published online by Cambridge University Press

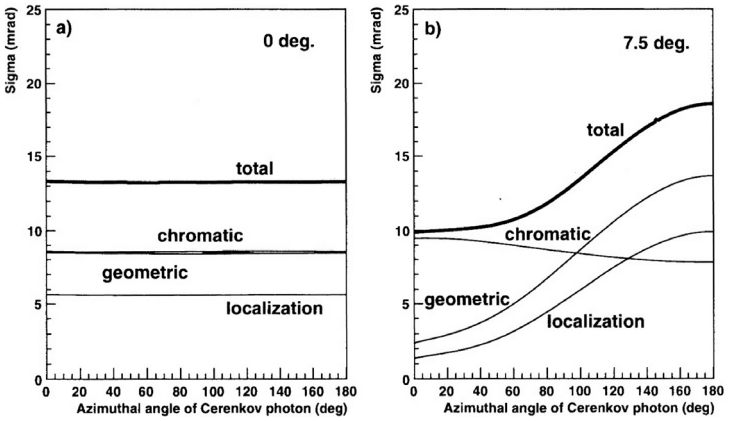

Figure 14.8 Cherenkov angle error due to several dispersive factors, for two values of the particle incidence angle (Nappi and Seguinot, 2005). With kind permission of Springer Science+Business Media.

14.3 First generation RICH detectors

The practical implementation of the RICH technology with gaseous detectors depends on solving two crucial issues: the conversion of photons into electrons by a suitable photo-ionizing agent, and the possibility of reaching gas gains high enough to detect single photoelectrons. As discussed in Section 8.10, due to the copious emission of UV photons by the avalanches, reconverting in the sensitive volume, the two requirements are conflicting. A solution was found in the late 1970s by operating the multi-step avalanche chamber structure with a triethyl amine (TEA)-rich gas mixture (Charpak and Sauli, 1978), see Section 8.10.

Owing to high vapour pressure of TEA, 55 torr at room temperature, Figure 14.10 (Anderson, 1988), the absorption length for UV photons is a few mm; detectors can therefore achieve a few ns time resolutions and operate at high event rates. Sensitive in the VUV region, between 7.5 and 9.5 eV with a calcium fluoride window, and thanks to the suppression of photon-induced feedback between the two amplification elements, the device can attain gains well above 10^5, adequate for fully efficient detection of single photoelectrons. The region of sensitivity restricts the choice of the main filling gas, which has to be transparent for the photons; a mixture of helium with 3% TEA was used in the detector described below.

Recording the avalanche charge on anodes and on cathode wires at an angle to the anodes with the methods described in Chapter 8, the detector can localize unambiguously multiple photoelectrons with sub-millimetre accuracy. Figure 14.11

https://doi.org/10.1017/9781009291200.016 Published online by Cambridge University Press

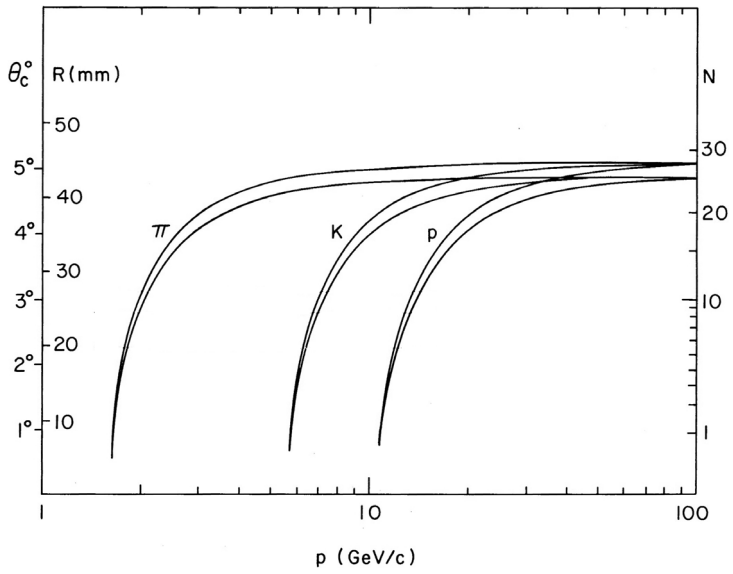

Figure 14.9 Example of computed resolution of a TEA-CaF_2 RICH detector with a 50 cm long, 10 atmosphere argon-filled radiator as a function of momentum (Charpak *et al.*, 1979a). By kind permission of Elsevier.

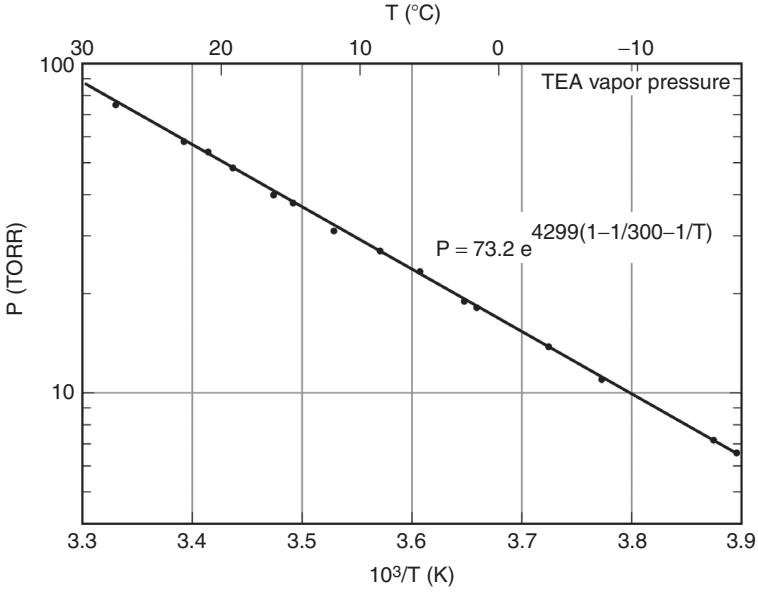

Figure 14.10 TEA vapour pressure as a function of temperature (Anderson, 1988). By kind permission of Elsevier.

https://doi.org/10.1017/9781009291200.016 Published online by Cambridge University Press

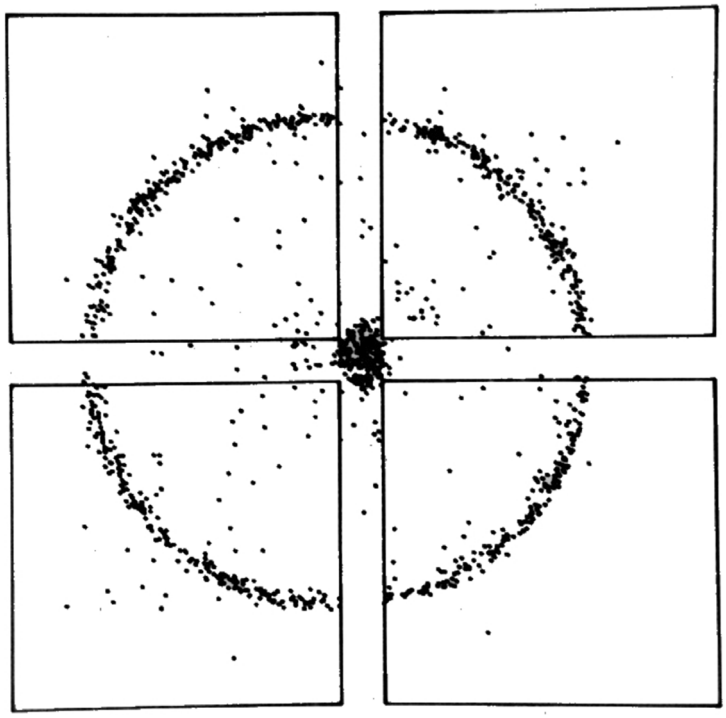

Figure 14.11 Overlapping Cherenkov rings detected with a TEA-filled multi-step chamber; the ring radius is 7 cm (McCarty *et al.*, 1986). By kind permission of Elsevier.

is an example of a ring image obtained by overlapping several hundred events produced by a proton beam in a helium-filled radiator, 8 m long, perpendicular to a multi-step chamber with an active surface of 20×20 cm^2. The squares are the boundaries of the composite four-crystal calcium fluoride window; the central region corresponds to the direct detection of the beam (McCarty *et al.*, 1986).

A large RICH detector of the described design was built and operated for many years for particle identification in the experiment E605 at FERMILAB (Adams *et al.*, 1983; McCarty *et al.*, 1986). Two identical multi-step chambers with 40×80 cm^2 active area, mounted on off-beam flanges of a 15 m long helium radiator, detect the photons reflected by a set of mirrors at the far end of the vessel; the calcium fluoride windows separating detector and radiator, assembled at CERN with a composite matrix of 32 crystals, are probably the largest CaF_2 windows ever built (Figure 14.12). Localization is performed by recording the signals on anodes and on groups of cathode wires at $\pm$ 45° to the anodes; Figure 14.13 shows a five-photon event, demonstrating the ambiguity-free reconstruction properties of the detector. Operated for many

https://doi.org/10.1017/9781009291200.016 Published online by Cambridge University Press

Figure 14.12 The large composite CaF_2 window of the E605 RICH. Picture CERN (1982).

years, with an average of 3.5 detected photons for saturated rings, the E605 RICH could identify pions from kaons up to 200 GeV/c; an early example of experimental ring radius distribution is shown in Figure 14.14 (McCarty *et al.*, 1986).

Alternatively to bulky gas radiators, and capable of identifying lower momentum particles, lithium and calcium fluoride can be used as radiators with the proximity focusing geometry. Owing to the large index of refraction of the crystals, however, photons emitted by near perpendicular particles undergo total internal reflection and are not detected. An elegant solution to the problem was developed for the CLEO III LiF-TEA ring imaging system, using an assembly of long, wedge-cut crystals arranged in a saw-tooth geometry; with around ten detected photons per ring, after thorough reconstruction taking into account the radiator geometry, a single photon angular resolutions of 12 mrad could be achieved (Mountain *et al.*, 1999; Artuso *et al.*, 2003).

14.4 TMAE and the second generation of RICH detectors

Despite their successful use in experiments, due to the sensitivity in the far UV domain, TEA-based photon detectors suffer from the described limitations in the choice of windows and radiators; they have also large intrinsic chromatic aberrations, which affect the resolution. Originally introduced in the 1980s to detect the

https://doi.org/10.1017/9781009291200.016 Published online by Cambridge University Press

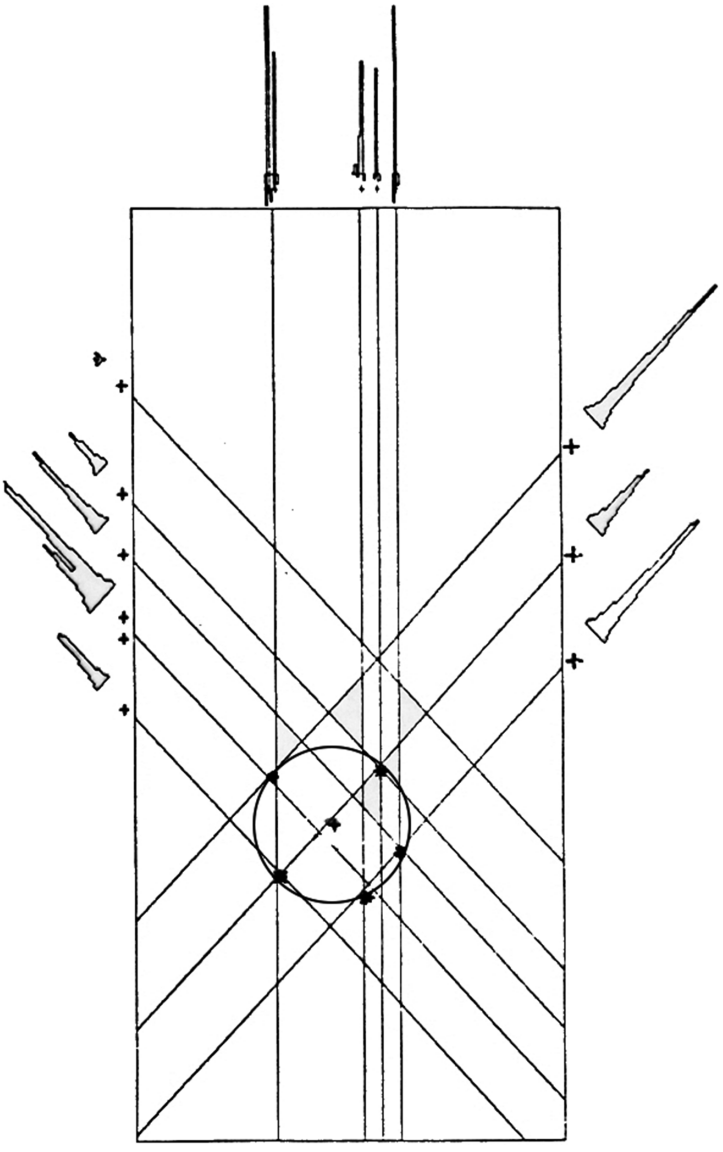

Figure 14.13 A five-photon ring detected in the E605 RICH (McCarty *et al.*, 1986). By kind permission of Elsevier.

photons emitted by the scintillation of xenon (Anderson, 1980), tetrakis dimethyl amino ethylene (TMAE),[2] thanks to its very low photo-ionization threshold, 5.3 eV, which permits the use of fused silica windows, TMAE represents a big step

[2] Colloquially pronounced 'Tammy', TMAE is part of a family of compounds spontaneously fluorescing by oxidation in air, developed as trackers for military applications. While this property imposes strict tightness requirements on detectors, it has been exploited to detect leaks in the detector.

https://doi.org/10.1017/9781009291200.016 Published online by Cambridge University Press

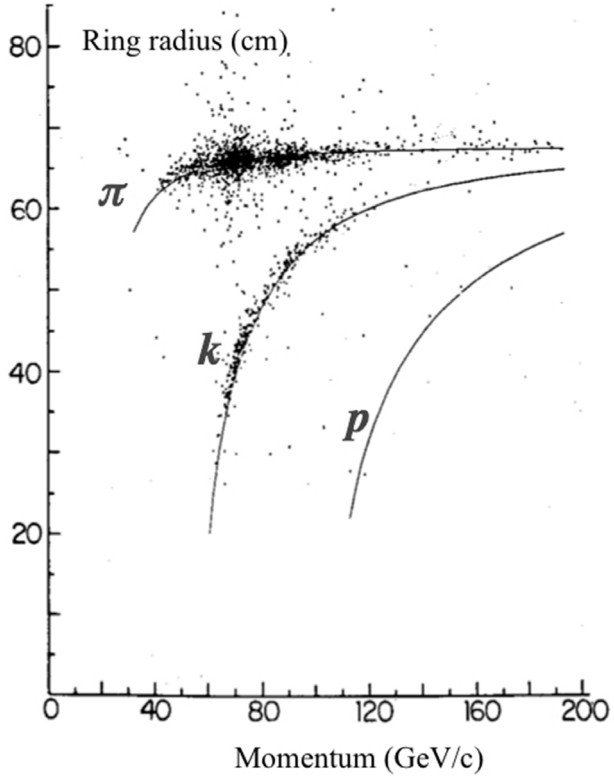

Figure 14.14 Particle identification power of the E605 RICH detector (McCarty *et al.*, 1986). By kind permission of Elsevier.

towards the realization of large acceptance RICH detectors. Other applications include detection of the fast component of BaF_2 scintillation for calorimetry (Anderson *et al.*, 1983; Anderson *et al.*, 1984) and positron emission tomography (Shotanus *et al.*, 1986; Miné *et al.*, 1988).

The main drawback of TMAE, aside from its chemical reactivity with oxygen and many materials, is its very low vapour pressure, thus requiring thick absorption gaps and/or high operating temperature to achieve good photon detection efficiency, Figure 14.15 (Anderson, 1988). Computed for a peak cross section of 30 Mb, Figure 14.16 provides the equivalent absorption length for the saturated vapour as a function of temperature; it is about 1 cm at 30°C. While this sets an intrinsic limit to the achievable time resolution, it was suitable for use in the forthcoming generation of colliding beam experimental systems. For historical surveys of TMAE-based RICH detectors see for example Buys (1996) and Engelfried (2011) as well as the proceedings of regular workshops dedicated to the subject.

https://doi.org/10.1017/9781009291200.016 Published online by Cambridge University Press

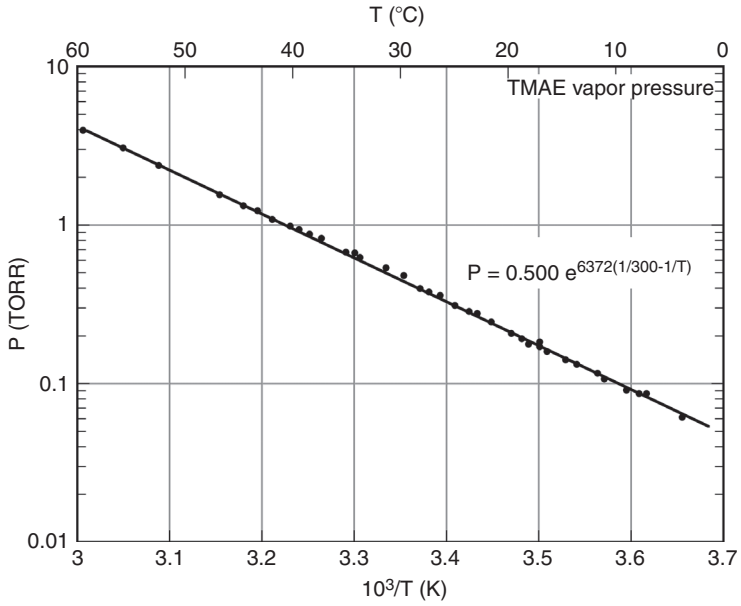

Figure 14.15 TMAE vapour pressure as a function of temperature (Anderson, 1988). By kind permission of Elsevier.

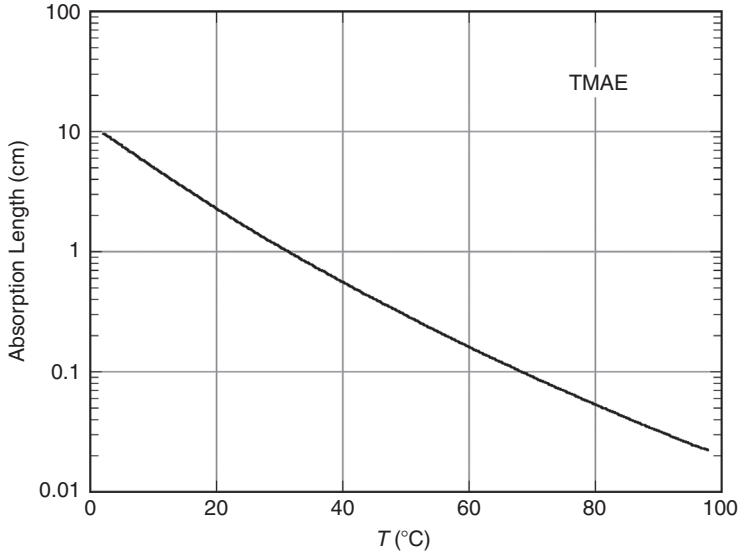

Figure 14.16 TMAE absorption length.

TMAE has been successfully used in detectors based on the multi-step chamber (Baur *et al.*, 1994). However, a two-dimensional time projection (TPC)-like drift chamber of the design shown in Figure 14.17, developed in the early 1980s, appeared more suitable to cover the large detection areas required by accelerator

https://doi.org/10.1017/9781009291200.016 Published online by Cambridge University Press

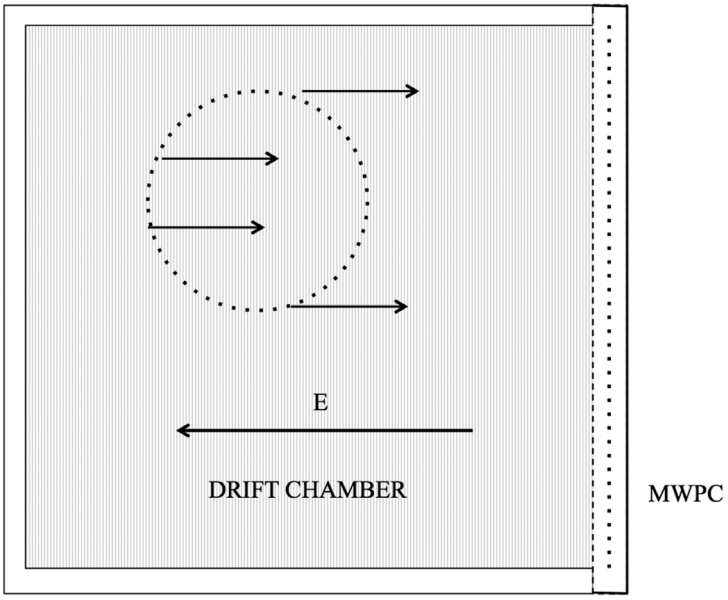

Figure 14.17 Schematics of the RICH TPC-like drift chamber.

experiments with moderate event rates (Ekelöf *et al.*, 1981; Barrelet *et al.*, 1982). Two sets of parallel wires or strips on the inner side of large fused silica windows define the drift gap. Photoelectrons created in the gas drift towards the end-cap detector, a multi-wire chamber; a thick conversion gap is needed to ensure good detection efficiency (5 cm in DELPHI). A measurement of the drift time on each wire permits one to reconstruct the ring pattern unambiguously; a coarse determination of the coordinate along the wire, obtained by recording the charge induced on cathode strips or by current division on the anodes, permits one to correct for the photon conversion depth in the gap.

First used at CERN's proton–antiproton collider for the UA2 experiment (Botner *et al.*, 1990), the TPC RICH concept was developed for the construction of the OMEGA fixed target spectrometer at CERN (Apsimov *et al.*, 1986), and the collider experiments SLD at SLAC (Ashford *et al.*, 1986; Abe *et al.*, 1998), DELPHI at LEP (Arnold *et al.*, 1988b; Arnold *et al.*, 1988a).

Similar in design and capable of identifying charged particles in a wide range of velocities, the DELPHI and SLD modules employ a single TPC photon detector between two radiators, as shown schematically in Figure 14.18. On the gas radiator side, a set of spherical mirrors reflects the photon ring through the upper quartz window of the drift chamber; on the lower side, thin liquid radiator boxes with quartz windows on the detector side generate a ring pattern by proximity focusing. Figure 14.19 shows the computed Cherenkov angle as a function of particle momentum for the gas and liquid radiators indicated in the insets.

https://doi.org/10.1017/9781009291200.016 Published online by Cambridge University Press

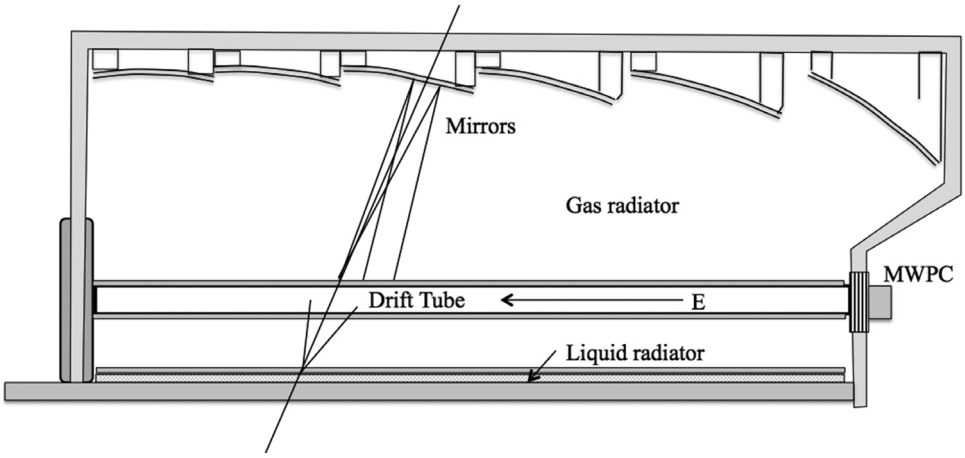

Figure 14.18 Schematics of the DELPHI barrel RICH (Arnold *et al.*, 1988b). By kind permission of Elsevier.

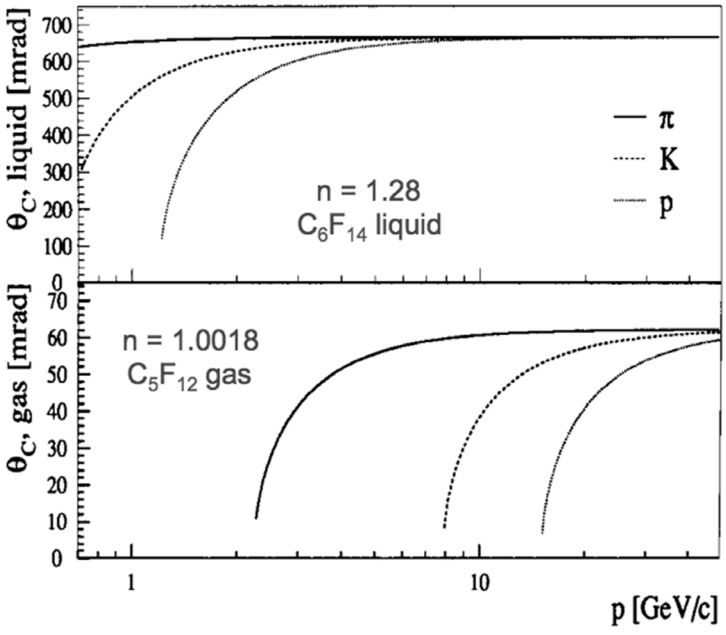

Figure 14.19 Cherenkov emission angles as a function of momentum for liquid and gas radiators (Adam *et al.*, 1996). By kind permission of Elsevier.

Due to the long photon absorption path in the low concentration photosensitive vapour, the gain achievable with the end-cap MWPC is limited by the appearance of secondary processes. Several detector geometries have been developed to limit the avalanche spread; Figure 14.20 shows two solutions, with sectored blinds

https://doi.org/10.1017/9781009291200.016 Published online by Cambridge University Press

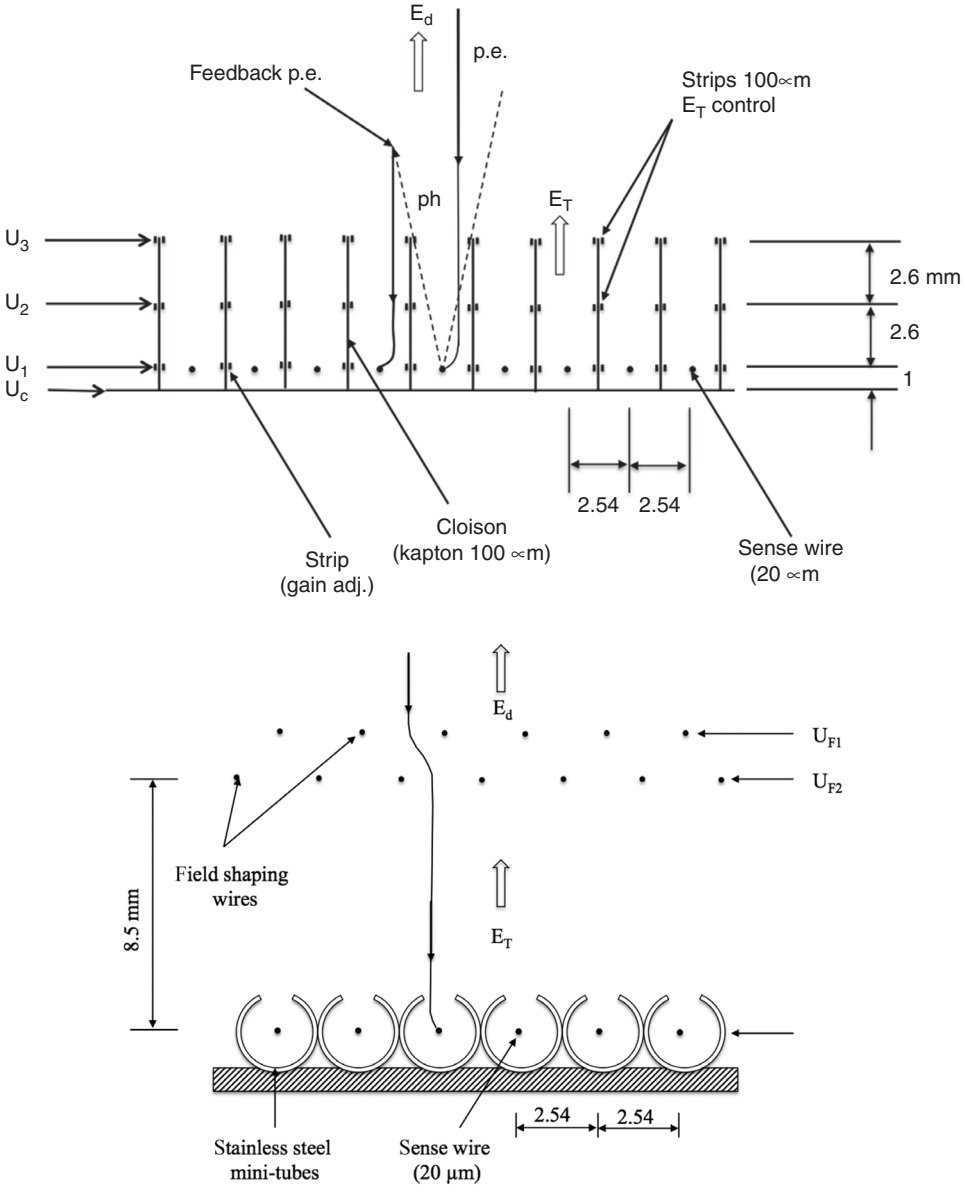

Figure 14.20 Photon feedback limiting structures: sectored blinds (top) and open-slit tubes (bottom) (Arnold *et al.*, 1986). By kind permission of Elsevier.

('cloisons') or sliced proportional tubes (Arnold *et al.*, 1986); geometry and electric field are designed so that all photoelectrons are collected by the anode wires, while the largest fraction of the photons emitted in the avalanches is absorbed by the walls. The first solution has been retained for most experiments.

https://doi.org/10.1017/9781009291200.016 Published online by Cambridge University Press

Figure 14.21 Two DELPHI barrel RICH TPC modules. Picture CERN (1986).

Figure 14.21 shows two 160 cm long modules of the DELPHI barrel RICH during construction, and Figure 14.22 the insertion of the 24-module full assembly into the mirror's barrel. After completion, the detector is installed horizontally between the time projection chamber and the magnet inner coil of the experiment.

Due to the detector geometry, for angled tracks the liquid radiator rings are in fact elongated hyperbola-like patterns, truncated at large angles by the total reflection in the liquid–window interfaces (Figure 14.23); the Cherenkov angle can be reconstructed by measuring the particle trajectory directly in the detector or in external devices (Arnold *et al.*, 1988b; Adam *et al.*, 1996; Erzen *et al.*, 1999). Figure 14.24 shows the single photon and ring radius angular resolutions measured for the liquid and gas radiators (Albrecht *et al.*, 1999); the particle identification capability of the detector is illustrated in Figure 14.25 (Schins, 1996).

A big effort was undertaken to refine the TMAE purification process needed to attain the desired quantum efficiency; its chemical reactivity with many materials has been studied in detail to permit the construction and long-term operation of detectors (Hallewell, 1994). The successful development of solid photocathodes, described in the next section, led to the dismissal of TMAE-based detectors.

14.5 Third generation RICH: solid caesium iodide (CsI) photocathodes

Compared to photo-ionizing gas fillings, a solid photocathode would have the advantage of an intrinsicly better time resolution due to the isochronous emission

https://doi.org/10.1017/9781009291200.016 Published online by Cambridge University Press

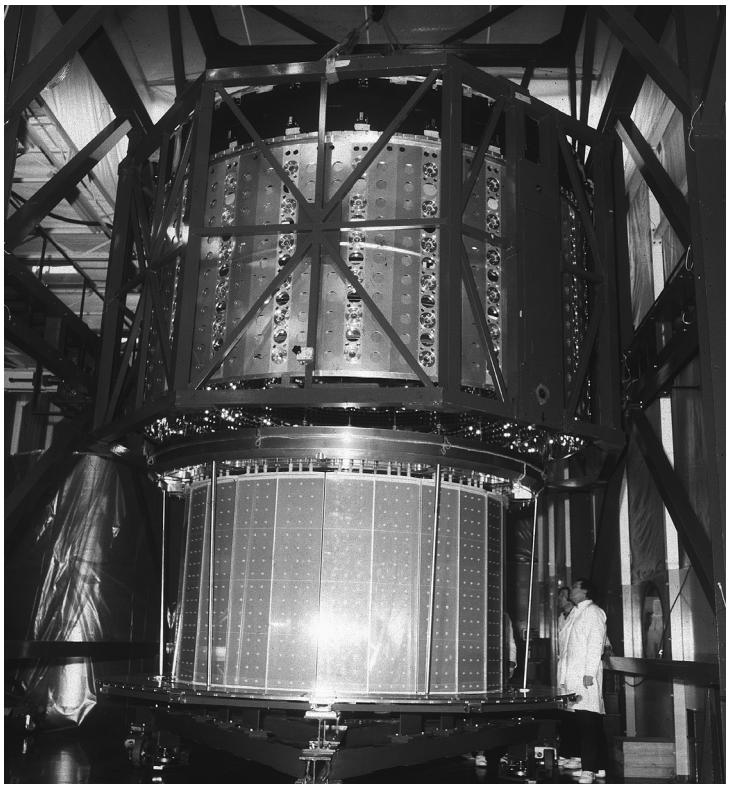

Figure 14.22 Insertion of the completed DELPHI RICH into the mirror barrel. Picture CERN (1986).

and collection of photoelectrons. The possibility of using a thin layer of caesium iodide (CsI), which has a 5.9 eV photo-ionization threshold, was discussed in the early works on RICH detectors (Arnold *et al.*, 1992). However, due to the reactivity of CsI with oxygen and water, it took several years to develop the appropriate deposition method, substrate kind and preparation and handling technologies to ensure high and uniform quantum efficiency in large area gaseous detector (Rabus *et al.*, 1999; Schyns, 2002 Braem *et al.*, 2003; Cisbani *et al.*, 2003). As shown by the example in Figure 14.26, the QE for the large areas required for HEP applications has been improved by a factor of two from the early measurements, approaching the values measured for monochromatic UV photons on small laboratory samples (Di Mauro, 2004). The CsI layer is deposited on the photocathodes by vacuum evaporation; although a brief exposure to air is known not to damage the layer, systems of leak-tight transfer boxes in argon are used to store the electrodes and mount them in the final detector assembly. A detailed description of the system developed for the production, handling and quality control of the large CsI photocathodes for the ALICE RICH is given in Hoedlmoser *et al.*, (2006).

https://doi.org/10.1017/9781009291200.016 Published online by Cambridge University Press

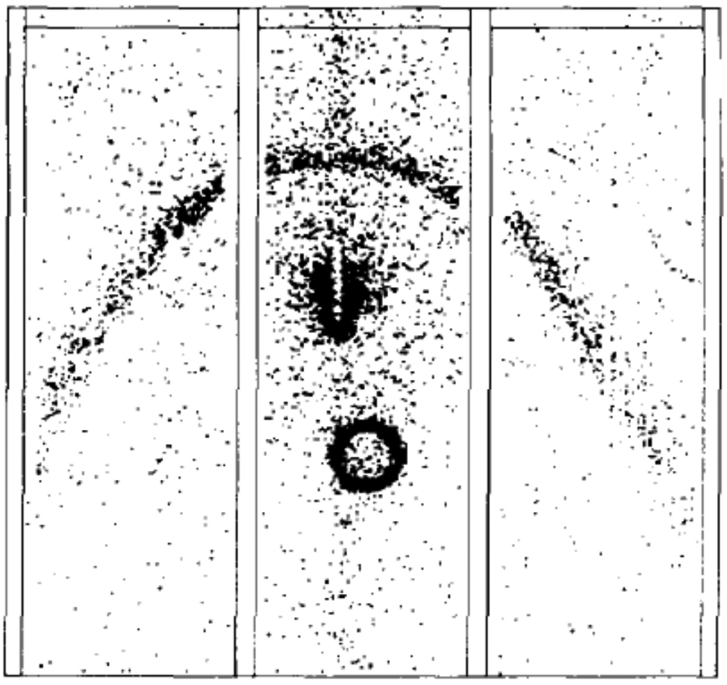

Figure 14.23 Superimposed image of 200 ring images for beam tracks at 18° with a prototype detector plane. The small ring and the elongated hyperbola are due respectively to the gas and the liquid radiators. The central scattered points are due to the beam (Arnold *et al.*, 1988b). By kind permission of Elsevier.

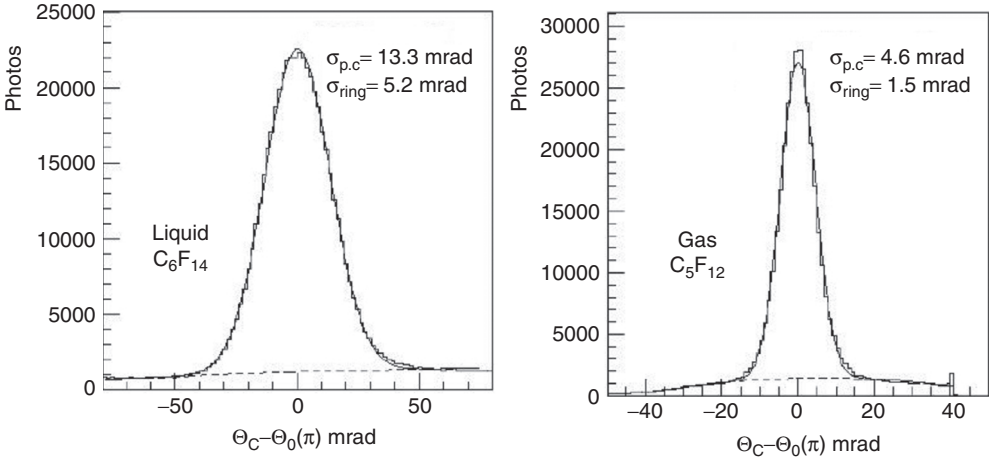

Figure 14.24 Cherenkov single photon and ring resolutions achieved with the DELPHI RICH (Albrecht *et al.*, 1999). By kind permission of Elsevier.

https://doi.org/10.1017/9781009291200.016 Published online by Cambridge University Press

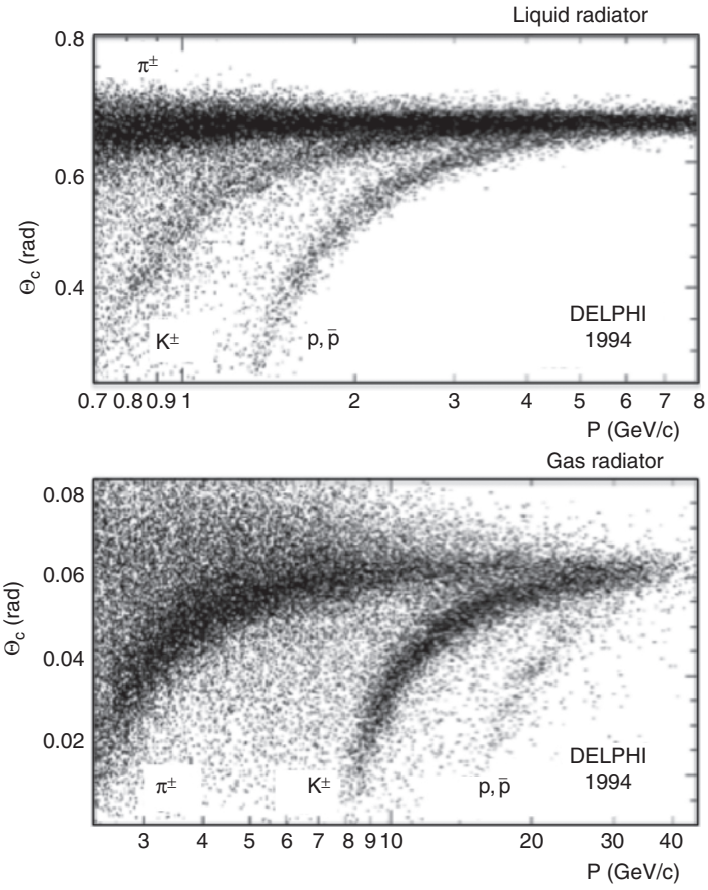

Figure 14.25 Particle identification as a function of momentum in the DELPHI barrel RICH for the liquid (top) and gas radiators (bottom). E. Schins personal communication (Schins, 1996).

CsI photocathodes can be deposited either as semi-transparent layers on the detector side of the window, or as reflective layers on the electrode facing the window. In the first case, the layer thickness has to be thoroughly controlled not to exceed the photoelectron capture length, around 100 Å; the second solution is preferred since it does not require a strict tolerance in the layer thickness. For a performance comparison between semi-transparent and reflective photocathodes see for example Lu and McDonald (1994).

The gas mixture used in the detector has to satisfy several requirements. The first is that the CsI layer is not damaged by exposure to the gas, thus imposing a strict control of the oxygen and water contaminants. For reflective photocathodes, as photons reach the layer through the gas gaps, the transparency should be close to 100% in the energy range between threshold

https://doi.org/10.1017/9781009291200.016 Published online by Cambridge University Press

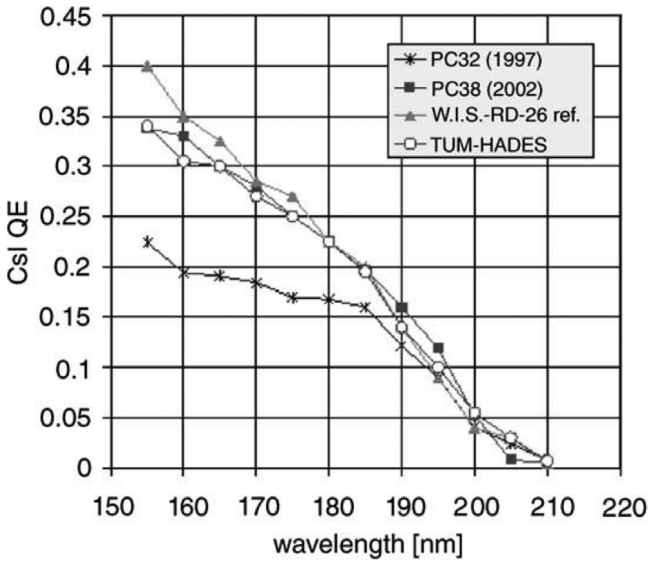

Figure 14.26 Improvement in quantum efficiency of large area CsI photocathodes (Di Mauro, 2004). Data are for the first ALICE prototype (PC32), the production modules ALICE (PC38) (Friese *et al.*, 1999) and HADES (TUM) (Fabbietti *et al.*, 2003). The curve labelled RD-26 is the best value obtained for small samples (Breskin *et al.*, 1995). By kind permission of Elsevier.

and window cut-off; photon absorption curves for gases commonly used in counters were given in Section 3.4. Once produced, photoelectrons have to escape from the layer; the extraction efficiency is a function of the external electric field, and depends on the gas, as shown in Figure 14.27, providing the recorded photocurrent in a cell normalized to the value in vacuum (Breskin *et al.*, 2002).

For mixtures including noble gases, due to their large electron backscattering cross sections, losses are considerable even at very high values of the field (Coelho *et al.*, 2007b). Despite the safety concerns caused by its flammability, methane has been adopted as gas filling by most experiments since it provides near-vacuum extraction at moderate values of the field; moreover, it permits one to reach the gas gains required to detect single photoelectrons, and it is fully transparent in the desired region of wavelength. The use of carbon tetrafluoride, which would solve the safety issues, raises concerns about the long-term damages induced by fluorinated compounds released in the avalanches (see Section 16.4).

Possible alternatives using neon mixtures are compared with pure methane in Figure 14.28 (Azevedo *et al.*, 2010).

https://doi.org/10.1017/9781009291200.016 Published online by Cambridge University Press

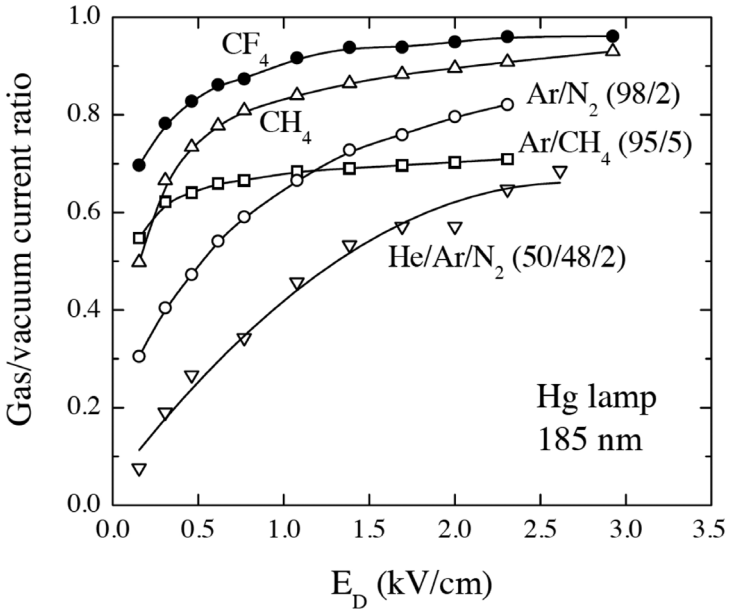

Figure 14.27 Ratio of photocurrent in different gases to that in vacuum as a function of field for CsI (Breskin *et al.*, 2002). By kind permission of Elsevier.

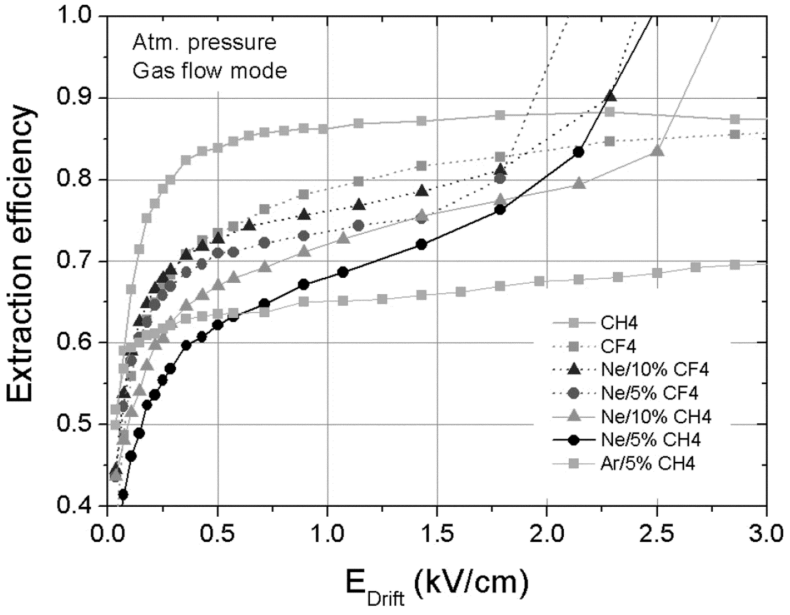

Figure 14.28 Photoelectron extraction efficiency in neon- and argon-based mixtures (Azevedo *et al.*, 2010). © IOP Publishing Ltd and Sissa Medialab srl. Reproduced by kind permission of IOP Publishing.

https://doi.org/10.1017/9781009291200.016 Published online by Cambridge University Press

14.6 CsI-based RICH particle identifiers

CsI-based gaseous photon detectors have been operated in many experimental setups; for comprehensive reviews see Piuz (2003) and Dalla Torre (2011). Differing in the detailed geometry and choice of the radiator, these systems share a common design of the detector, an MWPC with the photosensitive layer deposited on the cathode facing the window (Figure 14.29); a mesh in contact with the window serves the purpose of collecting the direct ionization of the particles. In proximity focusing systems, where the liquid radiator is in contact with the window, the distance between the MWPC and upper mesh is larger, up to 10 cm, to increase the size of the ring. In most cases, pure methane at atmospheric pressure is used as gas filling.

Due to the expected multiplicity of the events (several rings with many photoelectrons), a projective readout is generally unsuitable; the readout plane is then segmented into a matrix of pads individually instrumented. Photoelectrons extracted from the CsI layer drift to the anodes and multiply in avalanche, thus inducing a charge distribution on the cathode pads; the geometry and size of the pads are chosen to permit a centre of gravity interpolation of the recorded charge and improve the coordinate determination.

The COMPASS RICH-1 detector is shown schematically in Figure 14.30. Two sets of CsI-MWPCs are mounted on a large volume gas radiator; the mirror array reflects the ring images on the detector planes, situated outside the high flux region of the primary beam (Albrecht *et al.*, 2003). Figure 14.31 is an example of a multiple ring pattern recorded with the detector, and Figure 14.32 shows the particle identification capability of the instrument (Abbon *et al.*, 2007).

Named the high momentum particle identification detector (HMPID), the ALICE proximity focusing RICH device deploys seven CsI-MWPC modules surrounding the interaction region at CERN's LHC; each module mounts six CsI-coated 64×40 cm^2 photocathode panels, segmented into pads of 8×8.4 mm^2.

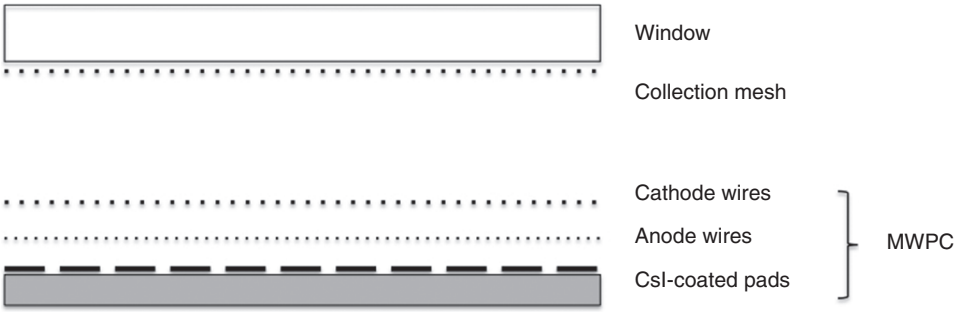

Figure 14.29 Schematics of the photon detector with a CsI photocathode.

https://doi.org/10.1017/9781009291200.016 Published online by Cambridge University Press

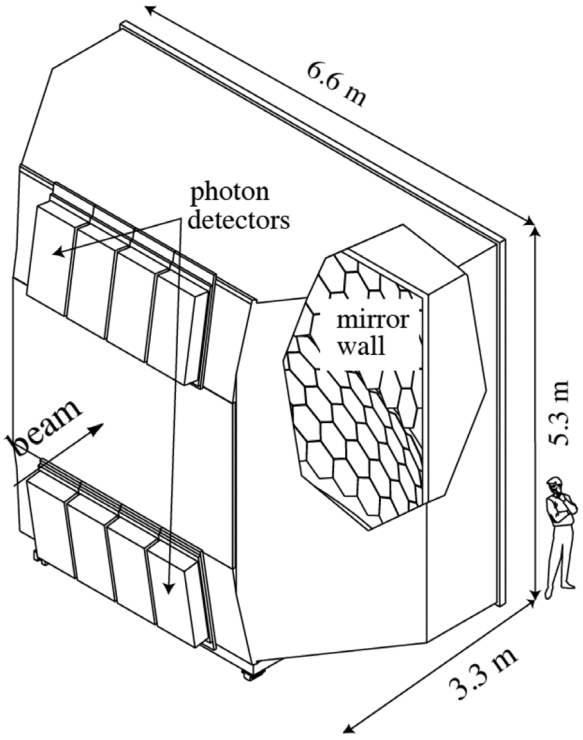

Figure 14.30 Artist's view of the COMPASS RICH-1 detector (Albrecht *et al.*, 2003). By kind permission of Elsevier.

Full-scale prototypes of the ALICE HMPID were tested both at CERN and in the STAR experiment at RHIC in Brookhaven. With a 15 mm thick perfluorhexane (C_6F_{14}) radiator, close to twenty reconstructed photon hits per ring are observed at saturation; Figure 14.33 is a single-track event display recorded in a test beam run (Cozza *et al.*, 2003). Most events share the charge between adjacent pads, as shown by the shades of grey in the picture, permitting interpolation. The resolution of the reconstructed ring radius is about 3 mrad (De Cataldo *et al.*, 2011).

Successfully operating in the ALICE experiment, but limited for particle identification to about 5 GeV by the use of high refractive index radiators, the detector is getting upgraded, adding a mirror-focused gas radiator to extend the useful range of momentum up to 10–30 GeV (Volpe *et al.*, 2008; Di Mauro *et al.*, 2011).

14.7 Micro-pattern based RICH detectors

While they are potentially capable of achieving a better time resolution than gas-phase photon detectors, experience has shown that MWPC-based CsI devices

https://doi.org/10.1017/9781009291200.016 Published online by Cambridge University Press

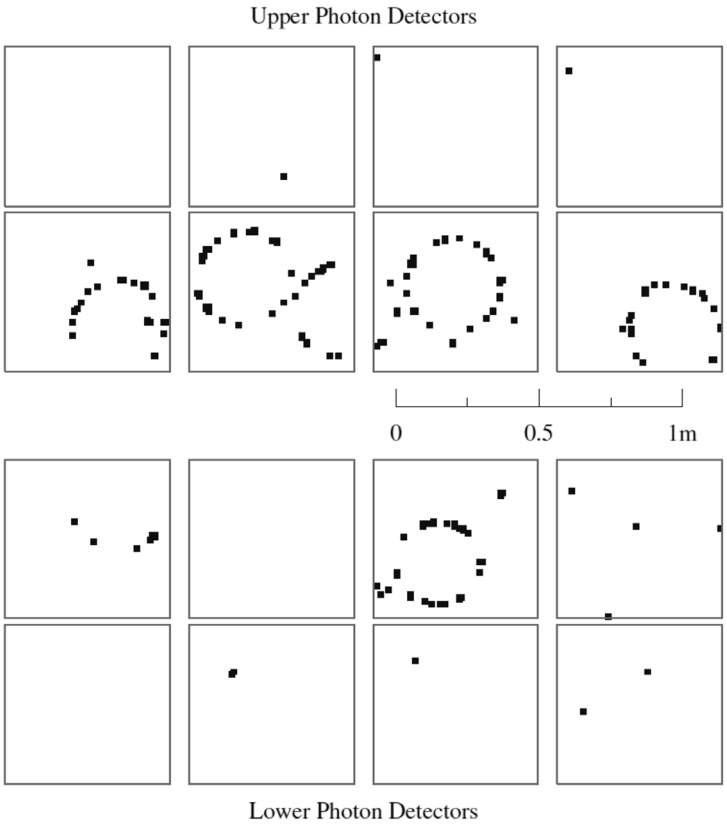

Figure 14.31 A multi-ring event recorded with the COMPASS RICH-1 (Abbon *et al.*, 2007). By kind permission of Elsevier.

suffer from a number of limitations affecting their performance. The use of a gas filling transparent to UV photons and the open MWPC geometry do not prevent photons emitted by the avalanches from reaching the photocathode, thus imposing a limit on the maximum gain that can be safely reached; as a consequence, relatively slow, low noise amplifiers have to be used, partly losing the fast intrinsic detector response. As observed in the COMPASS RICH, after a discharge induced by local defects, the detectors have a long-term memory of the event, preventing for days the application of the full voltage (Albrecht *et al.*, 2005). Even in the best operating conditions, pronounced long-term photocathode degradations have been observed and attributed to the bombardment by the ions produced in the avalanches (Hoedlmoser *et al.*, 2007). The cathode-induced signal readout method also sets a limitation on the two-photon separation, typically of several cm. The advent of the new generation of micro-pattern gas detectors, and in particular of the gas electron

https://doi.org/10.1017/9781009291200.016 Published online by Cambridge University Press

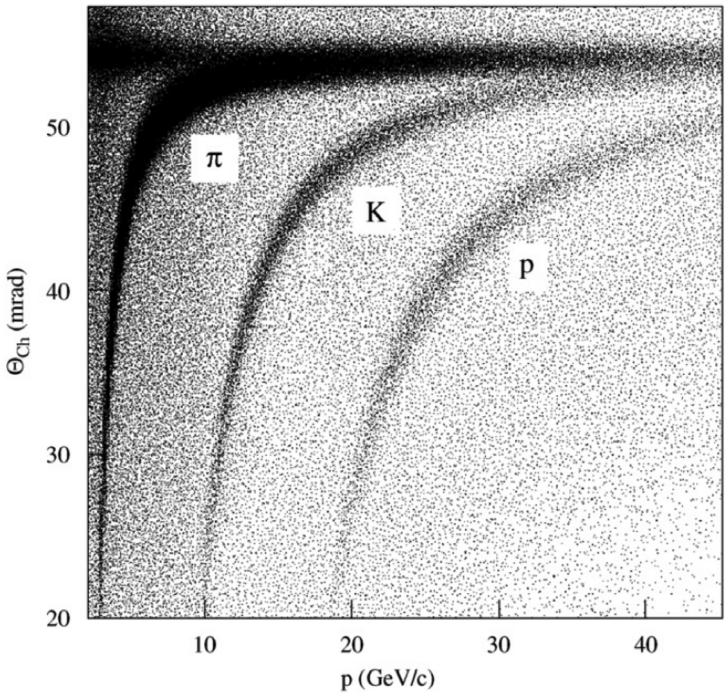

Figure 14.32 Particle identification power of the COMPASS RICH-1 (Abbon *et al.*, 2007). By kind permission of Elsevier.

multipliers (Chapter 13), opened up the possibility of developing better performing RICH devices.

Figure 14.34 shows schematically a GEM detector having the upper surface of the first electrode coated with a CsI photosensitive layer (Meinschad *et al.*, 2004); photoelectrons extracted from the layer are pulled by the applied field into the nearest hole, where a first step of charge amplification occurs. One or more GEM foils in cascade then permit one to attain the gain needed for detection, even in pure noble gases and their mixtures, an essential property in view of the realization of sealed counters (Buzulutskov *et al.*, 2000).

The device has several potential advantages. As most of the multiplication occurs in the last step of a multi-GEM structure, photons emitted by the avalanches cannot reach the photocathode and induce secondary processes. Only a minor fraction of the ions (those produced in the first stage of multiplication) hit the photocathode; using a small reverse electric field in the first gap, most primary ionization goes undetected. As in standard multi-GEM detectors, the amplified electron charge is directly collected on patterned electrodes, and can provide sub-mm position resolution. Due to the constant collection time, the intrinsic time resolution, if not degraded by the readout electronics, is of a few ns (Mörmann *et al.*, 2003).

https://doi.org/10.1017/9781009291200.016 Published online by Cambridge University Press

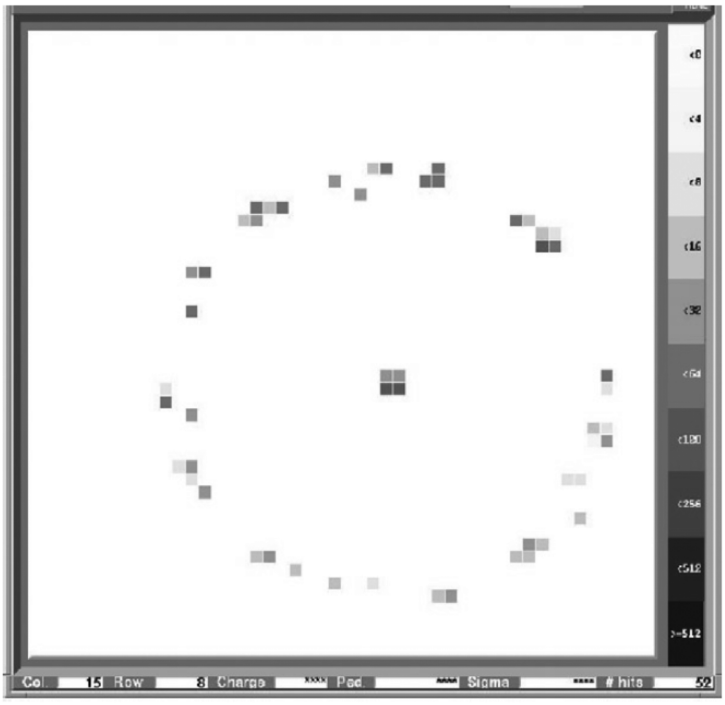

Figure 14.33 High momentum pion Cherenkov ring in the ALICE HMPID (Cozza *et al.*, 2003). By kind permission of Elsevier.

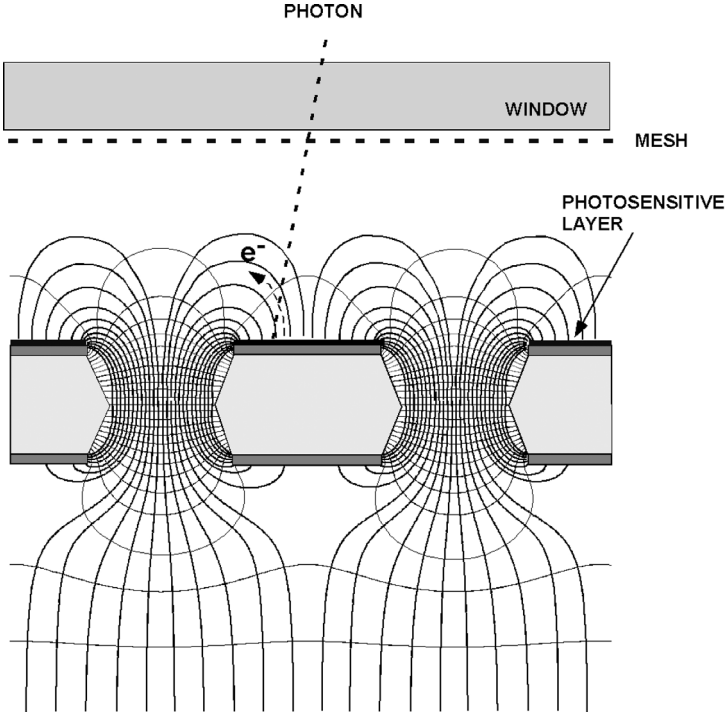

Figure 14.34 CsI-coated GEM detector (Meinschad *et al.*, 2004). By kind permission of Elsevier.

https://doi.org/10.1017/9781009291200.016 Published online by Cambridge University Press

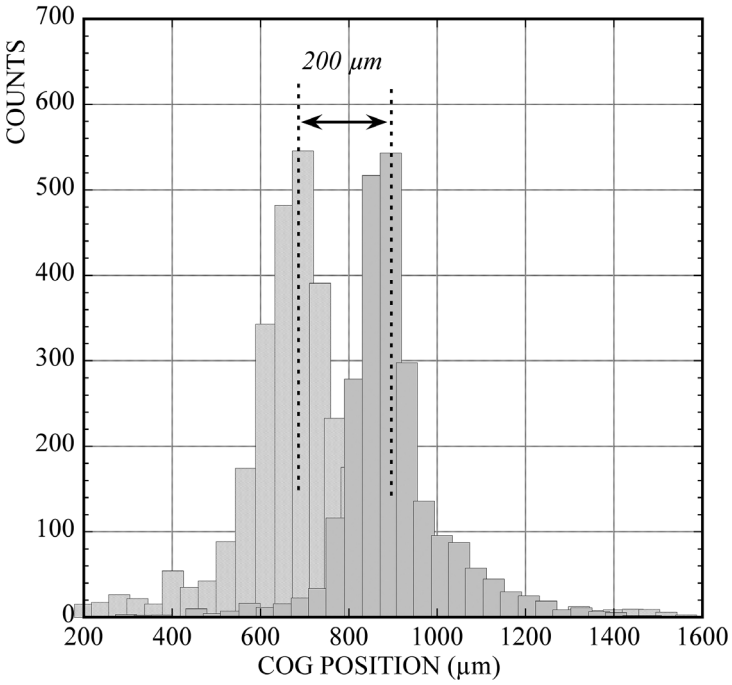

Figure 14.35 Position resolution measured with a CsI-GEM for two collimated photon beams 200 μm apart (Meinschad *et al.*, 2004). By kind permission of Elsevier.

Efficiency and localization properties of CsI-coated multi-GEM detectors have been studied in detail in view of possible applications for RICH detectors (Sauli, 2005). Figure 14.35 is an example of the position resolution measured for two collimated UV photon beams recording the collected charge on 200 μm wide strips on the anode of a triple-GEM detector (Meinschad *et al.*, 2004). The distributions have 200 μm FWHM, corresponding to the estimated width of the beam.

The hadron-blind detector (HBD), operated in the PHENIX experiment at RHIC, is the first large device making use of a CsI-coated GEM (Fraenkel *et al.*, 2005). It consists of a large gas volume acting as Cherenkov radiator, directly mounted in a windowless configuration on a triple-GEM with the photosensitive electrode facing the radiator. A reverse electric field applied to the volume collects the direct ionization; photons emitted by charged particles are detected and localized by a pad matrix on the anode. As shown schematically in Figure 14.36, the HBD has a semi-circular geometry, with radial radiators and detectors aimed at the interaction point (Anderson *et al.*, 2011). Thanks to the choice of the radiator (CF_4 at atmospheric pressure) the instrument efficiently detects the photons emitted by electrons and positrons, while the heavier hadrons are below threshold, hence the name of the device.

https://doi.org/10.1017/9781009291200.016 Published online by Cambridge University Press

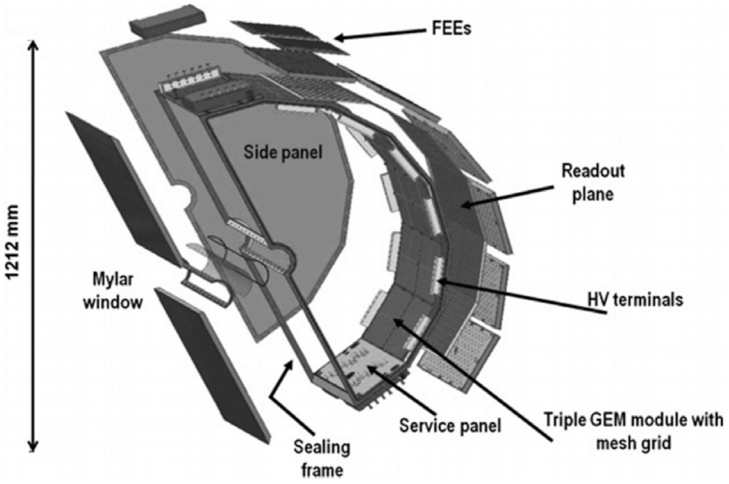

Figure 14.36 Schematic assembly of the HBD (Anderson *et al.*, 2011). By kind permission of Elsevier.

Manufactured on thin printed circuit board, the scaled-up thick GEM (TGEM, see Section 13.4) has the mechanical advantages of a rigid structure in view of the realization of large detector areas; optimization of performances and design show that gains sufficiently large for single photon detection can be obtained with a single multiplier (Alexeev *et al.*, 2011; Alexeev *et al.*, 2012).

Further reading

Ypsilantis, T. (1981) Cherenkov Ring Imaging. *Phys. Scripta* **23**, 371.
Nappi, E. and Seguinot, J. (2005) Ring Imaging Cherenkov Detectors: the state of the art and perspectives. *Riv. Nuovo Cimento* **28**, 1.

Selected conference proceedings

RICH2007 (2008) Sixth International Workshop on Ring Imaging Cherenkov Detectors, S. Dalla Torre, B. Gobbo and F. Tessarotto (eds.) *Nucl. Instr. and Meth*. **A595**, 1.
RICH2010 (2011) Seventh International Workshop on Ring Imaging Cherenkov Detectors, G. Hallewell, R. Forty. W. Hofmann, E. Nappi and B. Ratcliff (eds.) *Nucl. Instr. and Meth.* **A639**, 1.

https://doi.org/10.1017/9781009291200.016 Published online by Cambridge University Press